Inorganic Chemistry

Article

pubs.acs.org/IC

Iron(III) Phosphates Obtained by Thermal Treatment of the Tavorite-Type $FePO_4·H_2O$ Material: Structures and Electrochemical Properties in Lithium Batteries

Nicolas Marx,[†,⊥] Lydie Bourgeois,[‡] Dany Carlier,[†] Alain Wattiaux,[†] Emmanuelle Suard,[§] Frédéric Le Cras,[⊥] and Laurence Croguennec*[,†]

[†]CNRS, Université de Bordeaux, ICMCB, IPB-ENSCBP, 87 av. Schweitzer, 33608 Pessac cedex, France

[‡]Université de Bordeaux, Groupe de Spectroscopie Moléculaire, ISM, 351 cours de la Libération, 33405 Talence cedex, France

[§]Institut Laue-Langevin, 6 rue Jules Horowitz, 38000 Grenoble, France

[⊥]CEA LITEN, 17, av. des Martyrs, 38054 Grenoble cedex, France

Supporting Information

ABSTRACT: Thermal treatment of the Tavorite-type material $FePO_4·H_2O$ leads to the formation of two crystallized iron phosphates, very similar in structure. Their structural description is proposed taking into account results obtained from complementary characterization tools (thermal analyses, diffraction, and spectroscopy). These structures are similar to that of the pristine material $FePO_4·H_2O$: iron atoms are distributed between the chains of corner-sharing FeO_6 octahedra observed in $FePO_4·H_2O$ and the octahedra from the tunnels previously empty, in good agreement with the formation of a $Fe_{4/3}PO_4(OH)$-type phase. The formation of an extra disordered phase was also proposed. These samples obtained by thermal-treatment of $FePO_4·H_2O$ also intercalate lithium ions through the reduction of Fe^{3+} to Fe^{2+} at an average voltage of ~2.6 V (vs Li^+/Li), with a good cyclability and a reversible capacity around 120 mA h g^{-1} (>160 mA h g^{-1} during the first discharge).

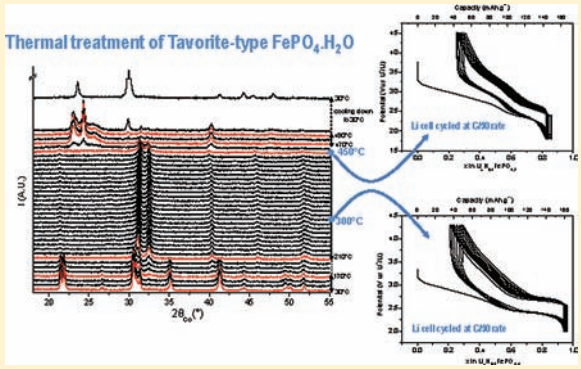

INTRODUCTION

Most of the researches performed in the field of positive electrode materials for lithium-ion batteries focus on the development of new materials. More than ten years ago with their work on $LiFePO_4$[1] Goodenough and co-workers paved the way for a new class of materials, the phosphates and more generally the polyanionic frameworks of transition metal ions. Very recently, a few groups (mainly those of Barker,[2−4] Tarascon,[5] Nazar,[6] and our group[7,8]) focused their interest on Tavorite-type materials $AM\{PO_4\}X$ (A = Li, H, ...) that are stabilized for several transition metal ions (M = Fe, Mn, V, etc.) and anions (X = O, OH, F). Depending on their composition it is possible to modify the potential of a given redox couple $M^{(n+1)+}/M^{n+}$ and as a consequence to tailor their properties as positive electrode in lithium batteries. This paper focuses on the formation of new phases from the thermal treatment of one of these Tavorite-type phases $FePO_4·H_2O$ (or $HFePO_4·H_2O$). The main message of this paper is probably that new phases, as also reported by Pralong et al. for instance for $FeSO_4·OH$,[9] can be obtained from exchange reaction or thermal treatment, these new materials being of interest as new compositions with new structures but also possibly as candidates at the positive electrode for lithium batteries.

As shown in Figure 1, $FePO_4·H_2O$ is characterized by chains of FeO_6 octahedra, interconnected through PO_4 tetrahedra,

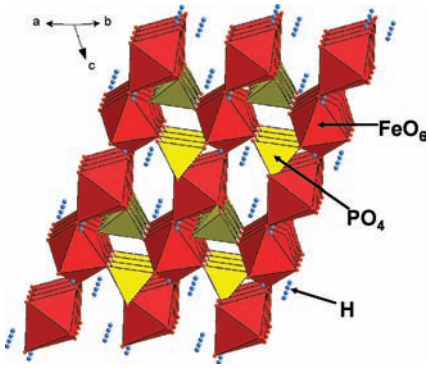

Figure 1. Representation of the $FePO_4·H_2O$ structure.

such that the resulting framework encloses different types of tunnels. Lithium intercalation was shown to occur through the reduction of Fe^{3+} to Fe^{2+} at an average voltage of ~2.8 V (vs Li^+/Li) with a

Received: December 6, 2011
Published: February 13, 2012

   dx.doi.org/10.1021/ic2026279 | *Inorg. Chem.* 2012, 51, 3146−3155

good cyclability. Dehydratation is not required before operation of $FePO_4 \cdot H_2O$ in lithium batteries because water is present as structural water: the oxygen of the OH_2 group belongs to the skeleton of the structure and in fact to the first coordination shell of the transition metal ions. Note that the electrochemical responses of other crystalline and amorphous $FePO_4 \cdot nH_2O$ were shown to be similarly interesting.[10−12] On the contrary, water adsorbed at the surface of an active material would be highly detrimental to its cyclability in lithium batteries as it would react with the salt ($LiPF_6$) of the electrolyte to form HF; similarly, water inserted in cavities of the host structure could be detrimental as it could be mobile (deinserted) upon cycling.

A thermogravimetric analysis (TGA) of $FePO_4 \cdot H_2O$, supported by in situ X-ray diffraction (XRD) and Raman scattering analyses, has revealed the formation of intermediate phases during the thermal treatment of $FePO_4 \cdot H_2O$ before the final formation of the quartz α-$FePO_4$. One of these phases was fully characterized from a structural point of view using X-ray and neutron diffraction analyses, as well as more local spectroscopic techniques such as Mössbauer and IR/Raman spectroscopies. First electrochemical results as positive electrode for lithium batteries will also be discussed.

EXPERIMENTAL SECTION

The $FePO_4 \cdot H_2O$ phase was obtained through a two-step synthesis, as described in detail elsewhere:[8] $LiFePO_4(OH)$ is synthesized first, using an hydrothermal process and then $FePO_4 \cdot H_2O$ is obtained through a Li^+/H^+ exchange. The obtained pale gray-green solid was heated up overnight in ambient air to a temperature between 300 and 450 °C, to get partially dehydrated samples.

The in situ high-temperature XRD experiments were carried out in ambient air on a PANalitycal X'pert Pro diffractometer (Co Kα radiation, and iron filter, antiscatter slit of 1° and divergence slit of 1/2° on the incident beam path) equipped with an Anton Paar HTK1200 high temperature chamber, with an alumina sample-holder. The diffraction patterns were recorded in the [18−55]° (2θ) angular range using an 0.0167° (2θ) step and a counting time of 1 h for each scan. The ex situ XRD patterns were collected on the same diffractometer, in the [5−120°] (2θ) angular range, with the same step but with a counting time of 24 h.

Neutron diffraction was performed at the Laue Langevin Institute (ILL) in Grenoble (France) on the high-resolution two-axis powder diffractometer D2B. The diffraction pattern was collected in transmission mode at room temperature with a wavelength of 1.5958(7) Å in the [0−160]° angular range using an 0.05° (2θ) step with an accumulation time of 4 h. The sample was contained in an 8 mm diameter vanadium tube. Because of the geometry of the neutron diffractometer, it was necessary to correct the absorption to take into account a decrease of the experimental diffracted intensity compared to the expected one. μ is the linear absorption coefficient of the sample and is defined as $\mu = n/V\Sigma_i n_i \sigma_i$ where n is the number of formula units in the unit cell, V the cell volume, n_i the number of a given atom in the formula unit, and σ_i the sum of coherent and incoherent scattering cross sections for the i-th atom. R is the radius of the vanadium cylinder. The X-ray and neutron diffraction patterns were analyzed by the Rietveld method as implemented in the FullProf program.[13]

Fe and P elemental analyses were performed after complete dissolution of the powder into a hydrochloric acid solution, using a Varian 720-ES Optical Emission Spectrometer (ICP-OES). A gas chromatography analysis was also performed with a Thermo Fisher Flash EA1112 CHNS analyzer, to quantify the amount of hydrogen in our samples. The water content was determined through a TGA, using a TA Instruments Q600 thermogravimetric analyzer.

Infrared spectroscopy measurements were performed using a FTIR Thermo Optek Nicolet 6700. The spectrometer was equipped with a DTGS detector and with a Ge-coated KBr or a solid substrate beamsplitter to access the middle and far-infrared regions. The sampling technique chosen was diffuse reflectance, which allows the study of powder or rough surface. To prevent any distortion of the signal because of its strong dependence on sample granulometry, the material to analyze (∼1 wt %) was mixed with cesium iodide (CsI) powder (transparent in middle and far-infrared 200−4000 cm^{-1}), previously dried at 400 °C overnight and finely ground. Finally, reflectance spectra were treated using the Kubelka−Munk law, which converts the reflectance to a signal proportional to the absorption coefficient. All these data were confirmed by attenuated total reflectance (ATR) that does not required any specific sample preparation.

Raman scattering measurements were performed with a Horiba Jobin Yvon Labram HR-800 microspectrometer. Spectra were recorded using a 514.5 nm excitation wavelength of an Ar^+ laser, with a power adjusted to 1 mW to avoid any degradation of the sample. No specific sample preparation was needed. For the in situ Raman scattering experiment carried out in ambient air, a very small quantity of material was heated from 30 °C up to 480 at 10 °C min^{-1}, with steps of 10, 20, or 30 °C, depending of the evolution of the spectrum. Before each measurement, a 10 min stabilization time was observed, and the focalization of the laser was checked.

Mössbauer spectroscopy studies were done on a Hadler spectrometer. The sample contained in average 10 mg of Fe per cm^2. The measurements were performed at room temperature in transmission geometry with a constant acceleration spectrometer using a ^{57}Co source in a Rh matrix. The velocity was calibrated by using pure iron metal as standard material at room temperature. All isomer shifts reported in this work refer to the natural α-Fe at 293 K.

For the evaluation of its electrochemical performance in laboratory lithium cells, the active material was first ball-milled with a (1:1) mixture of carbon black and graphite (1 g of active material with 210 mg of the carbon mixture during 30 min at 450 rpm), and then PTFE (polytetrafluoroethylene) was added as binder. The final composition of the positive electrode was approximately 80 wt % active material, 17 wt % carbon black/graphite (1:1), and 3 wt % PTFE. The resulting positive electrode was rolled into a thin sheet and cut into 0.64 cm^2 circular disks ($d \sim 40$ mg cm^{-2}). Metallic lithium was used as negative electrode and $LiPF_6$ (1M) in a mixture of ethylene carbonate (EC), propylene carbonate (PC), and dimethyl carbonate (DMC) in volume proportions 1:1:3 as electrolyte. The batteries were assembled in an argon-filled drybox (H_2O < 3 ppm) and cycled at room temperature in galvanostatic mode at a constant C/50 rate (corresponding to a theoretical exchange of one electron per formula unit during a charge or a discharge in 50 h).

RESULTS AND DISCUSSION

1. Thermal Analysis of $FePO_4 \cdot H_2O$ by TGA, XRD, and Raman Scattering. A TGA analysis presented in Figure 2 was performed on $FePO_4 \cdot H_2O$. The material was first heated at 2 °C/min up to 120 °C and maintained at this temperature during 12 h to evaporate the water molecules adsorbed at the surface of the particles. This preliminary weight loss corresponded to 0.54% of the total mass. Then the material was heated at 2 °C/min up to 800 °C. The global analysis, done under dry oxygen, revealed that $FePO_4 \cdot H_2O$ loses 10.94% of its weight in three steps: at first between 200 and 350 °C, then between 350 and 480 °C, and finally between 480 °C et 600 °C. Assuming that the global weight loss is associated to structural water, it corresponds to 1.03 H_2O per $FePO_4$ formula unit. The TGA curve shows clearly the existence of two intermediate hydrated phases of overall formula $FePO_4.\sim 0.37H_2O$ (obtained at ∼350 °C) and $FePO_4.\sim 0.09H_2O$ (obtained at ∼480 °C). The material obtained at high temperature, after the full dehydration of $FePO_4 \cdot H_2O$ (heated up to 800 °C and cooled down to room temperature), was identified as $FePO_4$ isostructural to quartz-α.

To follow the structural transitions and to identify the new phases formed during $FePO_4 \cdot H_2O$ heat-treatment, an in situ

dx.doi.org/10.1021/ic2026279 | Inorg. Chem. 2012, 51, 3146−3155

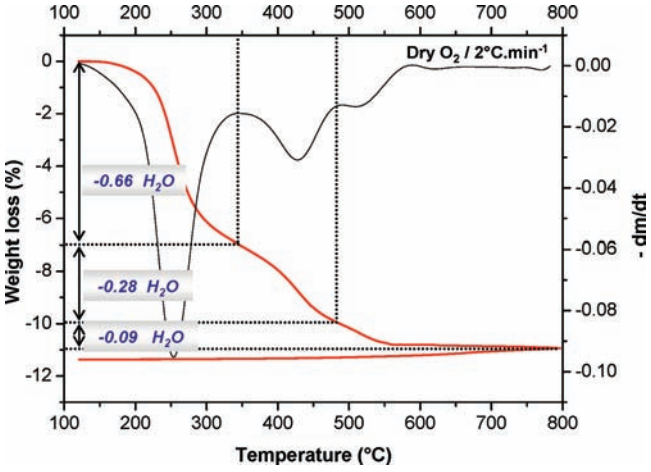

Figure 2. Weight loss curve (and its derivative) observed during the TGA under dry oxygen of the $FePO_4 \cdot H_2O$ material.

high-temperature XRD study was performed. The patterns thus obtained are presented in Figure 3. The $FePO_4 \cdot H_2O$ phase is stable up to about 170 °C, which is in agreement with the weight loss curve. A first temperature domain is then observed over a broad range (from 210 up to 450 °C), followed by a second temperature domain observed merely over a very restricted range (from 470 up to 490 °C). It turned out that it was very difficult to get a pure phase in the second temperature domain; it was always obtained as a mixture with a non-identified phase, the phase observed over the first temperature domain and quartz-α $FePO_4$. Therefore, only the first temperature domain will be characterized further. Above 500 °C, the quartz-α $FePO_4$ diffraction peaks keep on growing, the pure phase being obtained at about 550 °C. As expected the comparison of TGA and XRD data at a given temperature is not directly consistent as the temperature sweep rates are rather different in both experiments. The two temperature domains observed in TGA below 500 °C are not obvious in XRD. An enlargement of the two peaks observed in the angular range [30−33.5°] (2θ) of the in situ high-temperature XRD patterns obtained between 210 and 450 °C is given in the Supporting Information, Figure S1a. Change in the main peak's position ($2\theta \sim 31.2°$, Supporting Information, Figure S1b) and in the two peaks integrated surface area ($2\theta \sim 31.2°$ and $2\theta \sim 32.5°$) (Supporting Information, Figure S1c) shows the presence of three subdomains, represented by dotted lines. The first domain corresponds to the temperature range [210−230 °C], in which the main peak's position and the two peaks integrated surface area strongly varies, showing that the material still evolves. Then a second subdomain is observed in the temperature range [230−390 °C]: the main peak's position shifts slowly and continuously toward upper angles, which corresponds to a decrease in the corresponding interplane spacing and thus to a network contraction, whereas the two peaks integrated surface area also decreases slowly and continuously. It is important to keep in mind that in parallel, according to TGA analysis, the chemical composition evolves with the increasing temperature. A third subdomain is finally observed in the range [390−450 °C], in which drastic changes are observed again. Considering the temperature range [210−450 °C], another characteristic is observed: the appearance and disappearance of broad and small intensity peaks, at $2\theta \sim 27.5°$ and 30.2° (some other broad peaks are present on the patterns of ex situ synthesized materials at about $2\theta \sim 15.0°$, 19.3° and 39.5°, but those peaks are hardly visible in Figure 3). At 210 °C these peaks are not visible yet; they appear at ∼230 °C and remain observable until the temperature reaches 390 °C. Above 400 °C, they disappear again.

An in situ high-temperature Raman scattering experiment was performed in the same way, to follow the local structural modifications during thermal treatment in $FePO_4 \cdot H_2O$. As described in Figure 4, $FePO_4 \cdot H_2O$ was heated from room temperature up to 480 °C (maximum temperature limit of the oven), with steps of 10, 20, or 30 °C. The spectra were recorded between 150 and 4000 cm^{-1} but will be shown in the

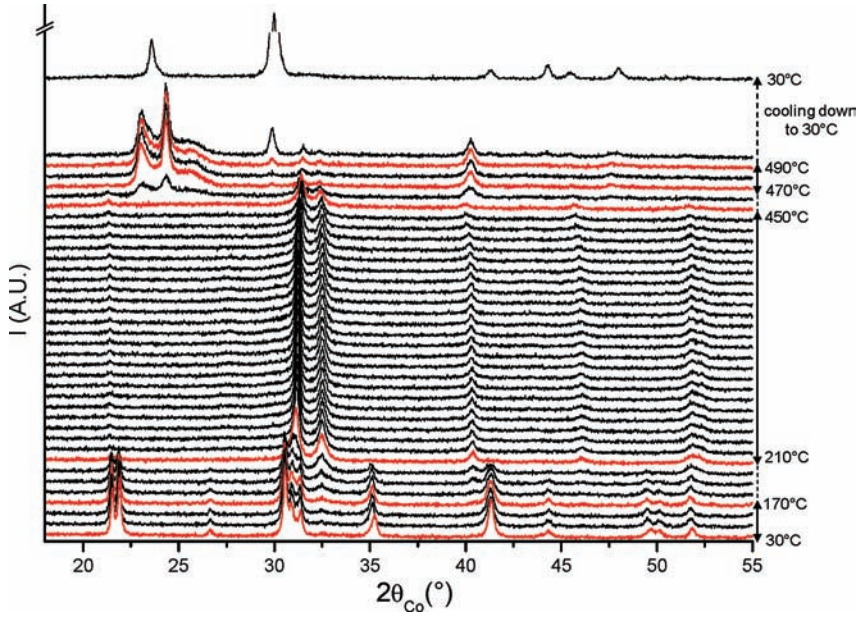

Figure 3. Patterns recorded during the in situ high-temperature XRD study of $FePO_4 \cdot H_2O$ (heating speed = 2 °C min^{-1} and waiting time of 10 min before each scan). The first two patterns were recorded at 30 and 150 °C, then every 10 °C up to 500 °C. Last pattern was recorded after cooling down to room temperature.

dx.doi.org/10.1021/ic2026279 | Inorg. Chem. 2012, 51, 3146−3155

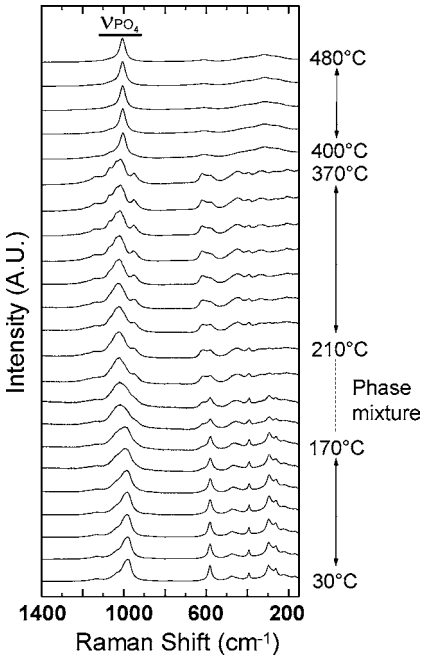

Figure 4. Raman spectra recorded during the in situ high-temperature analysis of $FePO_4{\cdot}H_2O$ (heating speed = 10 °C min^{-1} and waiting time of 10 min before each scan).

following only between 150 and 1400 cm^{-1}, domain where the spectral changes are the most visible. Three temperature domains are clearly observed: the first corresponds to the stability domain of $FePO_4{\cdot}H_2O$, it extends from room temperature up to 170 °C and is followed by an intermediate temperature range between 170 and 210 °C characterized by a mixture of phases; the second domain extends from 210 to 370 °C, and the third one above 400 °C. These Raman scattering data are in very good agreement with TGA analyses reported in Figure 2, but also with XRD data as highlighted in the Supporting Information, Figure S1a–c.

2. Composition and Structure of the Materials Obtained by Heat-Treatment of $FePO_4{\cdot}H_2O$ at 300 and 450 °C. *Synthesis.* Since the XRD pattern evolves drastically between room temperature and 210 °C, strong changes in the symmetry (space group) and in the structure of the material are expected. To characterize them precisely, it was necessary to synthesize samples ex situ and to collect their XRD patterns at room temperature. Two temperatures were chosen for the syntheses: 300 and 450 °C. They are characteristic of the two subdomains observed in the temperature range 210–450 °C and revealed through the fine analysis of the XRD patterns (Supporting Information, Figure S1), as well as that of the Raman spectra (Figure 4). In the following these two materials will be called *sample A* and *sample B*, respectively. $FePO_4{\cdot}H_2O$ powder was heated up to 300 °C (or 450 °C) in a tubular oven with a heating rate of 2 °C/min and then cooled down at 2 °C/min to room temperature. The materials thus obtained are perfectly stable at room temperature in air. Some changes in color were observed between the two powders: $FePO_4{\cdot}H_2O$ is a pale-green powder, the partially dehydrated sample obtained at 300 °C (sample A) remains pale-green, whereas that obtained at 450 °C (sample B) turns into yellow. Over 550 °C quartz α-$FePO_4$ is brown-red.

Chemical Analyses. To determine the difference in composition between the two materials, elemental (ICP) and thermogravimetric (TGA) analyses were performed. As expected, the heat-treatment of $FePO_4{\cdot}H_2O$ has no effect on the Fe/P ratio which remains constant and equal to 1. The TGA results are given in the Supporting Information, Figure S2. The two materials were heated up from 120 to 800 °C at 2 °C min^{-1} in dry oxygen: weight loss was 4.28% of the total mass for sample A and 2.58% for sample B, which represents respectively 0.37 and 0.22 H_2O per $FePO_4$. A gas chromatography analysis was also performed to quantify the amount of hydrogen remaining in those samples; it was shown to confirm the TGA results: these partially dehydrated materials contain around 0.48 wt % and 0.25 wt % of hydrogen which represents respectively 0.39(1) and 0.20(1) H_2O per $FePO_4$. According to these different analyses, sample A and sample B thus respectively correspond to $FePO_4{\cdot}{\sim}0.4H_2O$ (or $H_{0.8}FePO_{4.4}$) and $FePO_4{\cdot}{\sim}0.2H_2O$ (or $H_{0.4}FePO_{4.2}$). In the following, the two materials will thus be called sample A_$H_{0.8}FePO_{4.4}$ and sample B_$H_{0.4}FePO_{4.2}$.

Fe Mössbauer Spectroscopy Analysis. The two materials were analyzed by Mössbauer spectroscopy to get additional information about the iron atoms (oxidation state and environment). High-speed analyses ([−10 to +10 mm s^{-1}]) have shown that no divalent iron or magnetic impurity, such as Fe_2O_3, could be detected in the limit of the detection level. The spectra obtained for sample A_$H_{0.8}FePO_{4.4}$ and sample B_$H_{0.4}FePO_{4.2}$ are compared in Figure 5. The characteristic

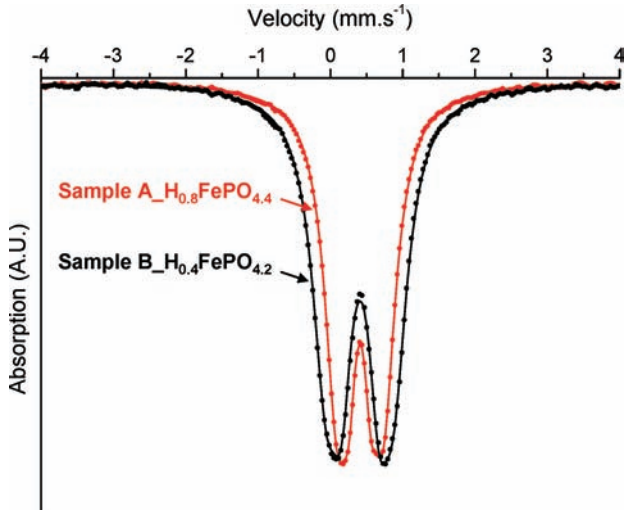

Figure 5. Comparison of Mössbauer spectra obtained for sample A_$H_{0.8}FePO_{4.4}$ (in red) and sample B_$H_{0.4}FePO_{4.2}$ (in black), presented in the velocity range [−4 to +4] mm s^{-1}.

parameters deduced from their refinement, the isomer shift (δ), the full width at half-maximum (Γ), and the quadrupole splitting (Δ), are given in Table 1. The spectrum of sample B_$H_{0.4}FePO_{4.2}$ obtained after a thermal treatment of $FePO_4{\cdot}H_2O$ at 450 °C is broader than that of sample A_$H_{0.8}FePO_{4.4}$ obtained after a thermal treatment at 300 °C. To get a good minimization of the difference between calculated and experimental spectra, and especially to take into account the slight asymmetry and the large width of the spectra, they were calculated as a distribution of quadrupolar doublets, the full width at half-maximum (Γ) being fixed to 0.25 mm s^{-1}. It was necessary to consider two distributions to explain these experimental spectra. The isomer shifts of 0.40 and 0.41 mm s^{-1}, close to that observed for the pristine phase $FePO_4{\cdot}H_2O$,[14] indicate

dx.doi.org/10.1021/ic2026279 | *Inorg. Chem.* 2012, 51, 3146–3155

Table 1. Fitted Mössbauer Parameters[a] Obtained for Sample A_$H_{0.8}FePO_{4.4}$[b] and Sample B_$H_{0.4}FePO_{4.2}$[c]

	DIS	δ (mm s^{-1})	Γ (mm s^{-1})	Δ (mm s^{-1})	%	site
sample A_$H_{0.8}FePO_{4.4}$	1	0.41	0.25	0.66	64	Fe^{3+}
	2	0.40	0.25	0.84	36	Fe^{3+}
sample B_$H_{0.4}FePO_{4.2}$	1	0.41	0.25	0.75	49	Fe^{3+}
	2	0.40	0.25	0.87	51	Fe^{3+}

[a] δ = isomer shift, Γ = full width at half maximum and Δ = median quadrupole splitting. [b] Obtained after a thermal treatment of $FePO_4{\cdot}H_2O$ at 300°C. [c] Resp. at 450°C.

that the two samples contain trivalent iron ions only, in oxygen octahedral environment.[15]

X-ray and Neutron Diffraction Analysis. These two materials were then analyzed by XRD; their patterns are compared in Figure 6. They are very similar, despite as already

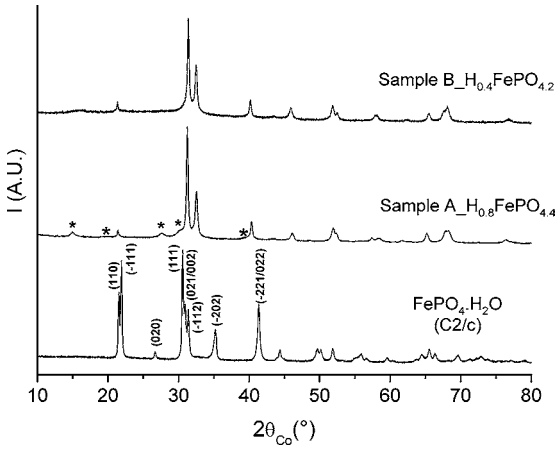

Figure 6. XRD patterns of the materials obtained after a thermal treatment of $FePO_4{\cdot}H_2O$ at 300 °C (sample A_$H_{0.8}FePO_{4.4}$) and 450 °C (sample B_$H_{0.4}FePO_{4.2}$).

mentioned the presence of extra small intensity and broad peaks at $2\theta \sim 15.0°$, 19.3°, 27.5°, 30.2° and 39.5° (marked by * in Figure 6) for sample A_$H_{0.8}FePO_{4.4}$. By analogy with phosphates reported in literature and showing an XRD pattern close to those observed in the temperature range [210−450 °C], two crystallographic cells could be considered to describe sample A_$H_{0.8}FePO_{4.4}$. The first one is of monoclinic symmetry and is described in the space group *C*2/*c*; it corresponds to the unit cell used to describe the structure of the iron hydroxyphosphate $Fe_4(PO_4)_3(OH)_3$.[16] The second one is of tetragonal symmetry and described in the space group $I4_1/amd$; it is similar to the unit cell used to describe $VPO_4{\cdot}H_2O$,[17] but also $Fe_{1.37}(PO_4)(OH)$[18] whose composition is very similar to that of $Fe_4(PO_4)_3(OH)_3$ mentioned above. Afterward, the two phases $Fe_4(PO_4)_3(OH)_3$ and $Fe_{1.37}(PO_4)(OH)$ will be described by the formula $Fe_{4/3}PO_4(OH)$, the first one being $Fe_{4/3}PO_4(OH)$ of monoclinic symmetry and the second one being $Fe_{4/3}PO_4(OH)$ of tetragonal symmetry. These two hydroxyphosphates have very similar structures. The phase of tetragonal symmetry is characterized by chains of $(Fe_{2/3}\square_{1/3})O_6$ octahedra sharing faces along *a* and *b* axes, as shown in Figure 7a. One third of these $(Fe_{2/3}\square_{1/3})O_6$ octahedral sites is empty and randomly distributed within the structure. The structure of monoclinic symmetry has a cell

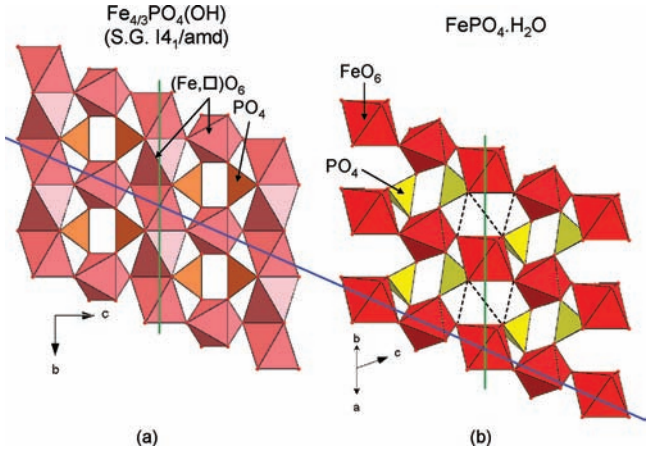

Figure 7. Comparison of the structures of $Fe_{4/3}PO_4(OH)$ (tetragonal symmetry) (**a**) with that of $FePO_4{\cdot}H_2O$ (**b**).

volume three times bigger than that of tetragonal symmetry, with the tripling of the *a* parameter that corresponds to the interchains distance. In that case the empty octahedral sites are ordered within the structure, with the succession of two FeO_6 octahedra and one $\square O_6$ octahedron along the chains. Note that the chains of corner-sharing octahedra highlighted by the blue line are also observed in $Fe_{4/3}PO_4(OH)$ as well as in $FePO_4{\cdot}H_2O$ as shown in Figure 7. The tunnels that are empty in $FePO_4{\cdot}H_2O$ are partially occupied by iron ions in octahedral environments in $Fe_{4/3}PO_4(OH)$.

To analyze the sample A_$H_{0.8}FePO_{4.4}$ XRD pattern by the Le Bail method by taking into account the broad and small intensity peaks, it was necessary to consider the triple unit cell described in the space group *C*2/*c*; the result is given in Figure 8a. The cell parameters thus obtained are a = 19.577(8) Å, b = 7.371(3) Å, c = 7.450(3) Å and β = 102.12(4)° (V = 1051.1(6) Å^3, V/Z = 87.6(1) Å^3). The volume per formula unit determined for this phase remains very similar to that of $FePO_4{\cdot}H_2O$ (V/Z = 87.0(1) Å^3): as reported in Table 2, this partially dehydrated material is characterized by smaller a (or $a/3$) and b parameters and by a larger c parameter. Nevertheless, the refinement is not satisfying since the profile evolution is not continuous as a function of the angle: as shown in inset in Figure 8a the majority of the diffraction peaks are rather narrow (fwhm ~0.25° (2θ)), whereas those corresponding to the superstructure are much broader (fwhm ~0.60° (2θ)). This difference in line broadening can thus not be well taken into account by a pseudo-Voigt profile function. No structural analysis through the Rietveld method was possible for this sample A_$H_{0.8}FePO_{4.4}$.

As described in Figure 8b, the cell of tetragonal symmetry described in the space group $I4_1/amd$, appears much more appropriate to refine the sample B_$H_{0.4}FePO_{4.2}$ XRD pattern: indeed, the extra peaks associated to the superstructure (marked by * in Figure 6) are not (or barely not) observed in Figure 8b. The cell parameters thus determined are $a = b$ = 5.212(2) Å and c = 12.852(6) Å (V = 349.1(3) Å^3, V/Z = 87.3(1) Å^3), with as shown in Table 2 a volume per formula unit very similar to that of $FePO_4{\cdot}H_2O$. This material was also analyzed by neutron diffraction. The obtained pattern was then refined by the Rietveld method, considering the structural model $((Fe)_{8d})_{2/3}\{(P)_{4a}((O(1))_{16h}\}(O(2)_{4b})$ used by Vaughey et al. and El Badraoui et al. to describe the vanadium phases $VPO_4{\cdot}H_2O$ and $V_{1.23}PO_4(OH)_{0.69}(H_2O)_{0.31}$,[17,19] as well as by Song et al. to

dx.doi.org/10.1021/ic2026279 | Inorg. Chem. 2012, 51, 3146−3155

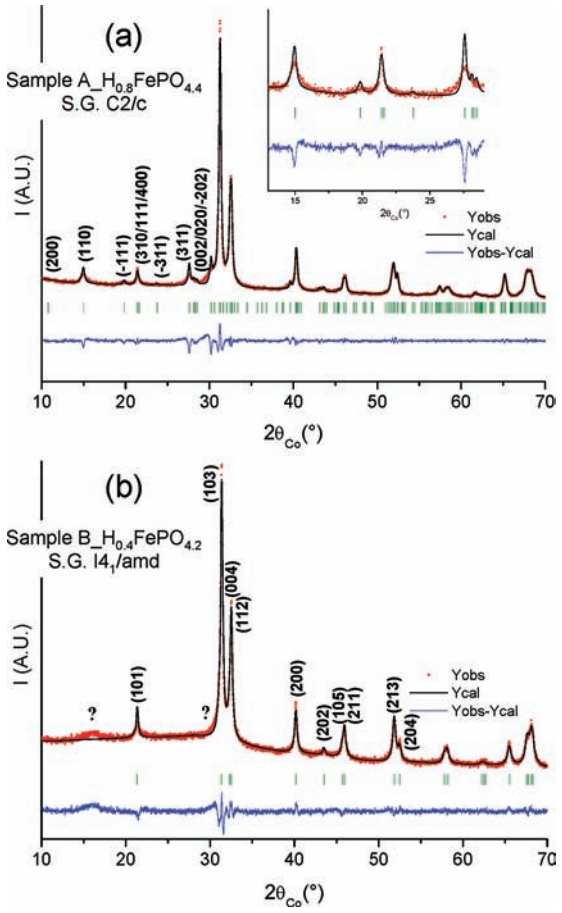

Figure 8. Comparison of the experimental and calculated XRD patterns of Sample A_$H_{0.8}FePO_{4.4}$ (**a**) and Sample B_$H_{0.4}FePO_{4.2}$ (**b**). The refinement was performed by the Le Bail method.

describe the iron phases $Fe_{1.19}(PO_4)(OH)_{0.57}(H_2O)_{0.43}$ and $Fe_{1.37}PO_4(OH)$.[18] The result of this refinement is given in Figure 9, 16 parameters were refined on the basis of 108 reflections; the final agreement parameters were R_{wp} = 15.1% and R_{Bragg} = 10.4%. As reported in Table 3, the refinement leads to an occupancy of 0.68(1) for the iron site 8d, that is, to a Fe/P ratio of about 1.36 and thus to the chemical formula $Fe_{\sim 4/3}PO_4(OH)$. The comparison of the phosphorus and iron environments in the two phases $Fe_{\sim 4/3}PO_4(OH)$ and $FePO_4{\cdot}H_2O$ is given in the Supporting Information, Table S1. These environments are significantly more distorted in $FePO_4{\cdot}H_2O$.

According to these results, the composition $Fe_{(4/3-x/3)}PO_4(OH)_{1-x}(OH_2)_x$ (with $0 \leq x \leq 1$)[18,19] could be proposed for these phases observed in X-ray and neutron diffraction and obtained by thermal degradation of $FePO_4{\cdot}H_2O$, that is, (in the limit of diffraction accuracy) with $x < 1$ for sample A_$H_{0.8}FePO_{4.4}$ and $x \sim 0$ for sample B_$H_{0.4}FePO_{4.2}$. According to these characterizations the composition of the phases observed in diffraction (with a Fe/P larger than 1) is not consistent with the global composition of the samples (i.e., $H_{0.8}FePO_{4.4}$ for sample A and $H_{0.4}FePO_{4.2}$ for sample B), so it suggests the presence of at least one additional disordered phase. Note that similar observations (i.e., thermal degradation of a phase with formation of disordered or even amorphous phases) were already

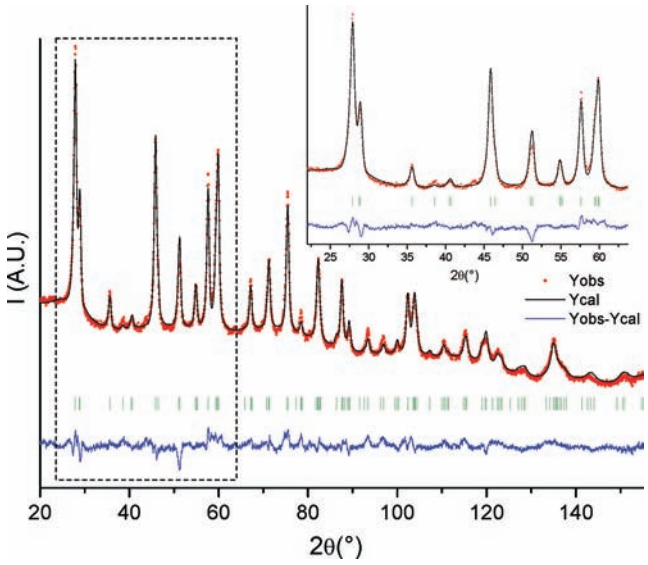

Figure 9. Comparison of the experimental and calculated neutron diffraction patterns of Sample B_$H_{0.4}FePO_{4.2}$. Enlargement of the plot in the range 22−63° (2θ) is given in inset.

Table 3. Structural and Profile Parameters Obtained by the Rietveld Refinement of the Neutron Diffraction Pattern Recorded for Sample B_$H_{0.4}FePO_{4.2}$

Sample B_$H_{0.4}FePO_{4.2}$						
space group: $I4_1/amd$						
$a = b$ = 5.212(2) Å				V = 349.1(3) Å^3		
c = 12.852(6) Å				V/Z = 87.3(1) Å^3		
atom	site		Wyckoff position		occupancy	B_{iso}
Fe	8d	0	0	1/2	0.68(1)	1.87(4)
P	4a	0	3/4	1/8	1	1.08(3)
O(1)	16h	0	0.507(4)	0.191(1)	1	2.83(4)
O(2)	4b	0	1/4	3/8	1	2.98(4)
Conditions of the Run						
wavelength					1.5953(1) Å	
temperature					300 K	
angular range					0° ≤ 2θ ≤ 160°	
number of points					3198	
zero-shift (2θ)					0.05(4)°	
number of fitted parameters					16	
Profile Parameters						
pseudo-Voigt function					η = 0.85(6)	
					U = 0.53(2)	
					V = −0.58(2)	
					W = 0.56(1)	
Conventional Rietveld R-Factors for Points with Bragg Contribution						
R_{wp} = 15.1%; R_{Bragg} = 10.4%; Scor = 4.6						

Table 2. Cell Parameters Obtained for the Materials Sample A_$H_{0.8}FePO_{4.4}$ and Sample B_$H_{0.4}FePO_{4.2}$ from the Refinement of Their XRD Patterns by the Le Bail Method, and Comparison with Those of the Pristine Phase $FePO_4{\cdot}H_2O$

material	space group	a (Å)	b (Å)	c (Å)	β (deg)	V (Å^3)	V/Z (Å^3)
$FePO_4{\cdot}H_2O$	$C2/c$	6.708(2)	7.761(2)	7.382(2)	115.08(2)	348.1(2)	87.0(1)
sample A_$H_{0.8}FePO_{4.4}$	$C2/c$	19.577(8)	7.371(3)	7.450(3)	102.12(4)	1051.1(6)	87.6(1)
sample B_$H_{0.4}FePO_{4.2}$	$I4_1/amd$	5.212(2)	5.212(2)	12.852(6)		349.1(3)	87.3(1)

dx.doi.org/10.1021/ic2026279 | Inorg. Chem. 2012, 51, 3146−3155

reported in the literature, especially for iron hydrated phosphates such as $FePO_4 \cdot nH_2O$.[20] To satisfy all the analyses performed, that is, a chemical formula with a Fe/P ratio smaller than 1 and iron atoms only at the trivalent state, the disordered (or amorphous) phase(s) is expected to contain for charge balance anionic groups such as HPO_4^{2-} or $H_2PO_4^-$.

IR Spectroscopy and Raman Scattering. Infrared spectroscopy and Raman scattering analyses of sample A_$H_{0.8}FePO_{4.4}$, sample B_$H_{0.4}FePO_{4.2}$, and the sample obtained after a thermal-treatment of $FePO_4 \cdot H_2O$ at 700 °C were performed, to determine the nature of the hydrogen containing groups (H_2O, OH, etc.). All the spectra were recorded in the range 200−4000 cm^{-1}, those corresponding to Raman scattering are given in Figure 10a and those for diffuse reflectance infrared

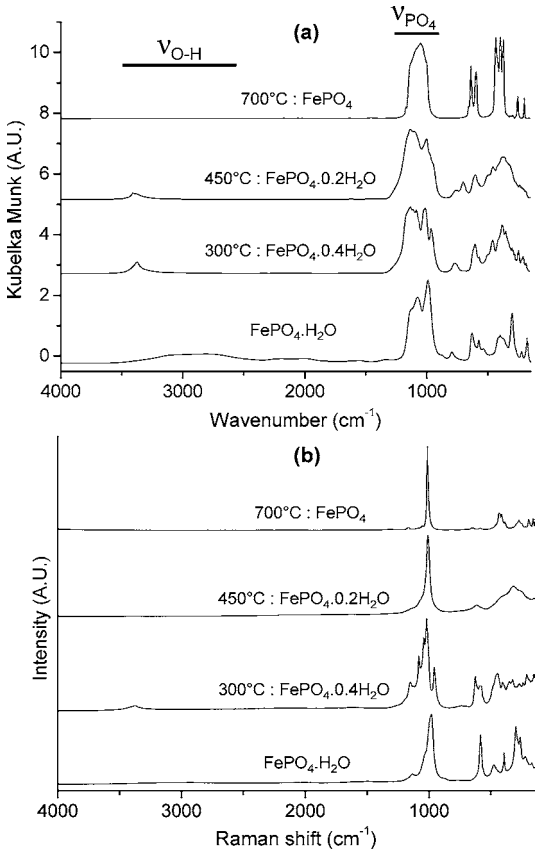

Figure 10. Spectra recorded for $FePO_4 \cdot H_2O$ and for the materials obtained after thermal treatment of $FePO_4 \cdot H_2O$ at 300 °C (sample A_$H_{0.8}FePO_{4.4}$), 450 °C (sample B_$H_{0.4}FePO_{4.2}$) and 700 °C (quartz-α type) in Raman scattering (**a**) and in infrared spectroscopy (diffuse reflectance) (**b**).

spectroscopy in Figure 10b. These Raman spectra are as expected similar to those obtained in situ during the thermal treatment of $FePO_4 \cdot H_2O$ and given in Figure 4. Only the two domains of particular interest for our study will be described in details in the following, that above 2300 cm^{-1} which is assigned to the O−H stretching bands and that between 900 and 1200 cm^{-1} which is attributed to the PO_4 stretching bands. One can already notice that there is no obvious contribution of an amorphous phase since the IR and Raman spectra do not show very broad bands (see Figures 4 and 10), as it would be expected in this case. In the following we will thus mention "disordered phase" rather than "amorphous phase".

To analyze more easily the spectra dominated by the PO_4 stretching bands, an analysis was performed for these modes by the correlation method, correlating the point group of the free PO_4 ion with the symmetry of the phosphorus site and the factor group of the material, for both $Fe_{4/3}PO_4(OH)$ (of monoclinic and tetragonal symmetry) and for $FePO_4$ (quart-α type) (as reported in Supporting Information, Tables S2 and S3). Theoretically, 12 IR-active and 12 Raman-active PO_4 stretching modes are expected for a monoclinic $Fe_{4/3}PO_4(OH)$ phase whereas only 2 IR-active and 3 Raman-active modes are expected for a tetragonal one. The number of PO_4 stretching bands observed in the IR and Raman spectra proves that the materials synthesized at 300 and 450 °C cannot be described by a pure tetragonal $Fe_{4/3}PO_4(OH)$ phase (Supporting Information, Table S3). In Raman scattering for example (Figure 10a), the number of bands obtained from the spectra deconvolution is four for $FePO_4 \cdot H_2O$,[8] at least seven for sample A_$H_{0.8}FePO_{4.4}$ and at least five for sample B_$H_{0.4}FePO_{4.2}$. These results are consistent with the possible presence of a monoclinic $Fe_{4/3}PO_4(OH)$ phase in sample A_$H_{0.8}FePO_{4.4}$ and seem to indicate an incomplete transition between the monoclinic phase (ordered) and the tetragonal phase (disordered) in sample B_$H_{0.4}FePO_{4.2}$. The IR spectra are consistent with these conclusions, which are also in good agreement with the XRD data analysis. Note that the IR and Raman spectra recorded for the sample obtained after a thermal treatment of $FePO_4 \cdot H_2O$ at 700 °C are compatible with quartz α-$FePO_4$ as reported in literature[21,22] and with the PO_4 stretching modes analysis given in Supporting Information, Table S3.

The evolution of the IR and Raman spectra in the region of the O−H stretching modes also provides some information. The spectra of the materials synthesized ex situ and given in Figure 10 show an evolution from a signal attributed to the presence of OH_2 groups in $FePO_4 \cdot H_2O$ (broad band in IR combined to an extremely weak signal in Raman scattering[8]) to a narrower signal situated at about 3400 cm^{-1} and revealing the presence of hydroxyl groups in sample A_$H_{0.8}FePO_{4.4}$ and sample B_$H_{0.4}FePO_{4.2}$. These changes were supported by the analysis of the in situ high-temperature Raman scattering spectra obtained during the continuous dehydration of $FePO_4 \cdot H_2O$ and reported in the 2800−4000 cm^{-1} domain in Figure 11; the three domains delimited by dotted lines correspond to the phase modifications observed upon increasing temperature. Some key spectra are compared in Figure 11a to highlight better their evolution in the region of the O−H stretching bands versus temperature; they reveal the appearance of a band typical of hydroxyl groups during the thermal treatment. Figure 11b gives the evolution of the integrated intensity ratio $I_{\nu_{OH}}/I_{\nu_{PO_4}}$ for the OH and PO_4 stretching bands as a function of temperature. Figures 11a−b show in a first step a continuous increase in the intensity of the OH groups' characteristic band, which is in good agreement with the formation of $Fe_{(4/3-x/3)}PO_4(OH)_{1-x}(OH_2)_x$ (with $0 \leq x \leq 1$). In the range of temperature associated with the monoclinic (ordered) phase, the intensity ratio $I_{\nu_{OH}}/I_{\nu_{PO_4}}$ increases up to 260 °C before decreasing. It suggests a decrease in the amount of the $Fe_{(4/3-x/3)}PO_4(OH)_{1-x}(OH_2)_x$-type phase, in good agreement with the results obtained from XRD (Supporting Information, Figure S1c). The comparison in Figure 10 of IR and Raman spectra obtained for materials synthesized ex situ shows that Raman scattering, which suggests the disappearance of the hydroxyl groups already at 450 °C

dx.doi.org/10.1021/ic2026279 | *Inorg. Chem.* 2012, 51, 3146−3155

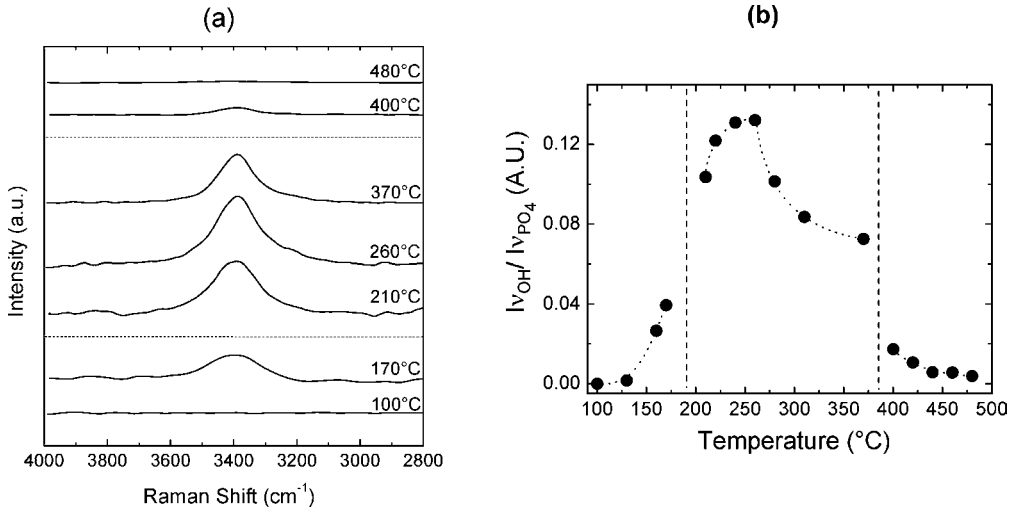

Figure 11. Enlargement of some key Raman spectra recorded during the in situ high temperature analysis of $FePO_4{\cdot}H_2O$ in the domain of the O−H stretching bands (2800−4000 cm^{-1}) (**a**) and evolution of the $I_{\nu_{OH}}/I_{\nu_{PO_4}}$ ratio (**b**). Note that changes in the intensity ratio can be compared only in a given temperature range; the proportionality factor between the $I_{\nu_{OH}}/I_{\nu_{PO_4}}$ and n_{OH}/n_{PO_4} ratios (where n is the number of groups) depends on changes in polarizability for these groups during vibrations, and thus on the phase considered. Since all the phases contained in these materials obtained by thermal treatment of $FePO_4{\cdot}H_2O$, especially the disordered phase(s), have not been clearly identified, only tendencies are given and discussed.

(Figure 11b), is less sensitive to these groups than IR spectroscopy, which reveals in good agreement with diffraction that the $Fe_{4/3}(PO_4)(OH)$ phase is still observed at 450 °C. Note also that the broadening of the low frequency modes observed at 450 °C (Figures 4 and 10) confirms the hypothesis of an order−disorder transition in the $Fe_{(4/3-x/3)}PO_4(OH)_{1-x}(OH_2)_x$ system.

Finally, concerning the "disordered" phase, IR spectroscopy and Raman scattering confirm the absence of Fe_2O_3,[23] consistently with the Mössbauer spectroscopy results. Furthermore, phases containing HPO_4^{2-} or $H_2PO_4^-$ groups, characterized by the presence of P−O stretching bands in the range 900−1200 cm^{-1} and O−H stretching bands at about 3350−3400 cm^{-1},[24] can contribute to the measured signal.

Combination of in situ and ex situ IR spectroscopy and Raman scattering analyses allowed us to prove that materials obtained by thermal treatment of $FePO_4{\cdot}H_2O$ at 300 and 450 °C are characterized by the appearance of OH groups, which reinforces the chemical formula proposed for the crystalline phase, that is, $Fe_{(4/3-x/3)}PO_4(OH)_{1-x}(OH_2)_x$ (with $0 \leq x \leq 1$). Furthermore, the presence of HPO_4^{2-} and $H_2PO_4^-$ groups is possible, as expected in the secondary "disordered" phase.

3. Electrochemical Properties in Lithium Cells of the Two Samples Obtained by Heat-Treatment of $FePO_4{\cdot}H_2O$ at 300 and 450 °C. Sample $A\_H_{0.8}FePO_{4.4}$ and sample $B\_H_{0.4}FePO_{4.2}$ were tested as positive electrodes in laboratory Swagelock-type lithium batteries; these materials have interesting theoretical capacities of 169 and 173 mA h g^{-1} respectively (corresponding to the full reduction of Fe^{3+} to Fe^{2+}, and the insertion of 1 Li^+ per formula unit). Figure 12a shows the evolution of the voltage versus the number of exchanged electrons in sample $A\_H_{0.8}FePO_{4.4}$, as well as the evolution in capacity during the first galvanostatic charge/discharge cycles performed between 1.8 and 4.5 V (vs Li^+/Li) at a C/50 rate. The first discharge curve can be divided in two parts: a first domain corresponding to the exchange of 0.6 electrons and to a fast continuous decrease in potential, and a second domain corresponding to the exchange of 0.35 electrons and to a slower decrease in potential. The average discharge potential is about 2.6 V (vs Li^+/Li) with a capacity of 160 mA h g^{-1} for the first discharge. At the end of the first cycle, an irreversible capacity loss of 30% is observed, but the capacity stabilizes at 120 mA h g^{-1} for the next cycles in non optimized conditions from the point of view of the electrodes and lithium electrochemical cells. It can also be noticed that the polarization is rather limited (∼ 200−300 mV). On subsequent cycles, the shape of the voltage curve remains unchanged, suggesting that the structure of the material obtained at the end of the first insertion is able to evolve reversibly during the following Li^+ insertion/deinsertion cycles.

In the same way, Figure 12b describes the evolution of the potential during the first galvanostatic charge/discharge cycles for sample $B\_H_{0.4}FePO_{4.2}$. The average potential, the loss of capacity, and the polarization are similar to sample $A\_H_{0.8}FePO_{4.4}$. The irreversible capacity loss is also close to 0.25 Li^+ per formula unit, those remaining trapped in the material. However, the shape of the stabilized voltage curve is quite different with a less marked plateau around 2,5 V/Li+/Li. Figure 12c compares the first discharge of both Li // sample $B\_H_{0.4}FePO_{4.2}$ and Li // sample $A\_H_{0.8}FePO_{4.4}$ cells in GITT mode (Galvanostatic Intermittent Titration Technique). It is interesting to notice that their discharge profiles are not similar: for Li // sample $B\_H_{0.4}FePO_{4.2}$ cells it starts at a slightly higher potential, which remains higher than that of Li // sample $A\_H_{0.8}FePO_{4.4}$ cells until 0.6 Li (per formula unit) have been inserted in both structures. Then, the potential of Li // sample $B\_H_{0.4}FePO_{4.2}$ decreases rather fast, whereas that of Li // sample $A\_H_{0.8}FePO_{4.4}$ decreases more slowly. Thus, at the end of the discharge, the potential of Li // sample $A\_H_{0.8}FePO_{4.4}$ is higher than that of Li // sample $B\_H_{0.4}FePO_{4.2}$.

According to the likely hypothesis for these samples of a mixture of phases, and since in addition an insertion of one lithium per formula unit is observed, the Fe^{3+} contained in the "disordered" phase is also necessarily reduced; the curves given in Figure 12 being the combination of electrochemical activity of both phases (ordered and disordered). Note that the electrochemical properties reported by Song et al.[18] for phases $Fe_{1.19}(PO_4)(OH)_{0.57}(H_2O)_{0.43}$ (Fe-60%) and $Fe_{1.37}PO_4(OH)$

dx.doi.org/10.1021/ic2026279 | Inorg. Chem. 2012, 51, 3146−3155

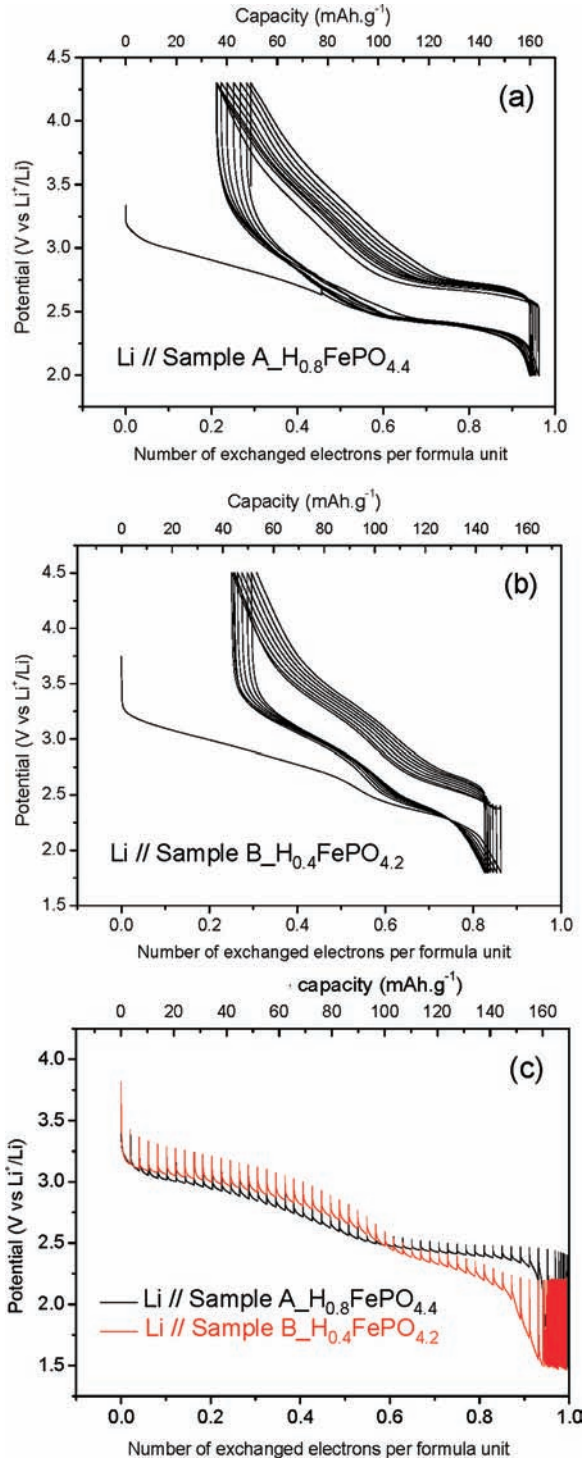

Figure 12. First electrochemical cycles obtained at C/50 rate for Li // Sample A_$H_{0.8}FePO_{4.4}$ (a) and Li // Sample B_$H_{0.4}FePO_{4.2}$ (b) and comparison between first discharges obtained in open circuit voltage conditions (C/50 rate, relaxation criteria: $dV/dt < 3$ mV/h) for both cells (c).

(Fe-2/3-T) obtained through hydrothermal synthesis are significantly different from those reported in Figure 12. For instance, the cycling curve observed for Fe-2/3-T shows a step in potential not observed for sample B_$H_{0.4}FePO_{4.2}$ and characterized by the presence of $Fe_{4/3}PO_4(OH)$, but also a "pseudo-plateau" at ~2.5 V (vs Li^+/Li) much more extended than that observed in our case. Our materials are thus different from those obtained by Song et al. by direct synthesis, and not by thermal degradation of $FePO_4 \cdot H_2O$ which leads to the formation of a mixture of phases, $Fe_{(4/3-x/3)}PO_4(OH)_{1-x}(OH_2)_x$ (with $0 \leq x \leq 1$) being the crystallized ones.

CONCLUSIONS

The thermal treatment of the Tavorite-type $FePO_4 \cdot H_2O$ material was shown to be an interesting synthesis route to prepare new hydroxy-phosphates $Fe_{(4/3-x/3)}PO_4(OH)_{1-x}(OH_2)_x$ (with $0 \leq x \leq 1$) whose structure remains closely related to that of the pristine material $FePO_4 \cdot H_2O$, with iron atoms distributed between the corner-sharing octahedra in the chains (initially fully occupied) and the octahedra in the tunnels (initially empty). These new materials were shown to intercalate lithium ions through the reduction of Fe^{3+} to Fe^{2+} at an average voltage of ~2.6 V (vs Li^+/Li), very similar to those observed for the Tavorite phases $LiFePO_4 \cdot OH$ and $FePO_4 \cdot H_2O$, and with a good reversibility and a stable capacity around 120 mA h g^{-1}.

ASSOCIATED CONTENT

Supporting Information

Further details are given in Figures S1–S2 and Tables S1–S3. This material is available free of charge via the Internet at http://pubs.acs.org.

AUTHOR INFORMATION

Corresponding Author

*Phone: +33 (0) 5 4000 2234 or +33 (0) 5 4000 2647. Fax: +33 (0) 5 4000 2761. E-mail: crog@icmcb-bordeaux.cnrs.fr.

Notes

The authors declare no competing financial interest.

ACKNOWLEDGMENTS

The authors would like to thank Gilles Le Flem (ICMCB) and Michel Couzi (ISM) for fruitful discussions, Philippe Dagault, Cathy Denage, and Laëtitia Etienne (ICMCB) for their technical assistance, ILL-Grenoble for neutron diffraction experiments, and CEA, ADEME, and Région Aquitaine for their financial support.

REFERENCES

(1) Padhi, A. K.; Nanjundaswamy, K. S.; Goodenough, J. B. *J. Electrochem. Soc.* **1997**, *144* (4), 1188–1194.
(2) Barker, J.; Saidi, M. Y.; Swoyer, J. L. *J. Eletrochem. Soc.* **2003**, *150*, A1394.
(3) Barker, J.; Saidi, M. Y.; Swoyer, J. L. *J. Eletrochem. Soc.* **2004**, *151*, A1670.
(4) Barker, J.; Gover, R. K. B.; Burns, P.; Bryan, A.; Saidi, M. Y.; Swoyer, J. L. *J. Electrochem. Soc.* **2005**, *152* (A), 1776.
(5) Recham, N.; Chotard, J.-N.; Jumas, J.-C.; Laffont, L.; Armand, M.; Tarascon, J.-M. *Chem. Mater.* **2010**, *22*, 1142.
(6) Ramesh, T. N.; Lee, K. T.; Ellis, B. L.; Nazar, L. F. *Electrochem. Solid-State Lett.* **2010**, *13*, A43.
(7) Marx, N.; Croguennec, L.; Carlier, D.; Suard, E.; Wattiaux, A.; Le Cras, F.; Delmas, C. *Dalton Trans.* **2010**, *39*, 5041.
(8) Marx, N.; Croguennec, L.; Carlier, D.; Bourgeois, L.; Pierre Kubiak, F.; Le Cras; Delmas, C. *Chem. Mater.* **2010**, *22*, 1854.
(9) Reddy, M. A.; Pralong, V.; Caignaert, V.; Varadaraju, U. V.; Raveau, B. *Electrochem. Commun.* **2009**, *11*, 1807.
(10) Masquelier, C.; Reale, P.; Wurm, C.; Morcrette, M.; Dupont, L.; Larcher, D. *J. Electrochem. Soc.* **2002**, *149*, A1037–A1044.
(11) Hong, Y. S.; Ryu, K. S.; Park, Y. J.; Kim, M. G.; Lee, J. M.; Chang, S. H. *J. Mater. Chem.* **2002**, *12*, 1870–1874.
(12) Song, Y.; Yang, S.; Zavalij, P. Y.; Whittingham, M. S. *Mater. Res. Bull.* **2002**, *37*, 1249–1257.

(13) Rodriguez-Carvajal, J. *FullProf*; Laboratoire Léon Brillouin: Saclay, France; http://www-llb.cea.fr/fullweb/powder.htm
(14) Marx, N., Ph.D. Thesis, University of Bordeaux, Bordeaux, France, December 17, 2010.
(15) Menil, F. *J. Phys. Chem. Solids* **1985**, *46* (7), 763.
(16) Torardi, C. C.; Reiff, W. M.; Takacs, L. *J. Solid State Chem.* **1989**, *82*, 203.
(17) El Badraoui, A.; Pivan, J. Y.; Maunaye, M.; Pena, O.; Louer, M.; Louer, D. *Ann. Chim. Sci. Mater.* **1998**, *23*, 97.
(18) Song, Y.; Zavalij, P. Y.; Chernova, N. A.; Whittingham, M. S. *Chem. Mater.* **2005**, *17*, 1139.
(19) Vaughey, J. T.; Harrison, W. T. A.; Jacobson, A. J. *Inorg. Chem.* **1994**, *33*, 2481.
(20) Reale, P.; Scrosati, B.; Delacourt, C.; Wurm, C.; Morcrette, M.; Masquelier, C. *Chem. Mater.* **2003**, *15*, 5051.
(21) Okada, S.; Yamamoto, T.; Okazaki, Y.; Yamaki, J.; Tokunaga, M.; Nishida, T. *J. Power Sources* **2005**, *146*, 570.
(22) Pasternak, M. P.; G.Kh. Rozenberg; Milner, A. P.; Amanowicz, M.; Zhou, T.; Schwarz, U.; Syassen, K.; Dean Taylor, R.; Hanfland, M.; Brister, K. *Phys. Rev. Lett.* **1997**, *79*, 4409.
(23) Zoppi, A.; Lofrumento, C.; Castellucci, E. M.; Sciau, Ph. *J. Raman Spectrosc.* **2008**, *39*, 40.
(24) Frost, R. L.; Weier, M. L.; Martens, W. N.; Henry, D. A.; Mills, S. J. *Spectrochim. Acta, Part A* **2005**, *62*, 181.